

Ground-based detection of G star superflares with NGTS

James A. G. Jackman,^{1,2★} Peter J. Wheatley,^{1,2} Chloe E. Pugh,^{1,2} Boris T. Gänsicke,^{1,2} Edward Gillen,³ Anne-Marie Broomhall,^{1,2,4} David J. Armstrong,^{1,2} Matthew R. Burleigh,⁵ Alexander Chaushev,⁵ Philipp Eig Müller,⁶ Anders Erikson,⁶ Michael R. Goad,⁵ Andrew Grange,⁵ Maximilian N. Günther,³ James S. Jenkins,^{7,8} James McCormac,^{1,2} Liam Raynard,⁵ Andrew P. G. Thompson,⁹ Stéphane Udry,¹⁰ Simon Walker,¹ Christopher A. Watson⁹ and Richard G. West^{1,2}

¹Department of Physics, University of Warwick, Gibbet Hill Road, Coventry CV4 7AL, UK

²Centre for Exoplanets and Habitability, University of Warwick, Gibbet Hill Road, Coventry CV4 7AL, UK

³Astrophysics Group, Cavendish Laboratory, J.J. Thomson Avenue, Cambridge CB3 0HE, UK

⁴Institute of Advanced Studies, University of Warwick, Coventry CV4 7HS, UK

⁵Department of Physics and Astronomy, Leicester Institute for Space and Earth Observation, University of Leicester, Leicester LE1 7RH, UK

⁶Institute of Planetary Research, German Aerospace Centre, Rutherfordstrasse 2, D-12489 Berlin, Germany

⁷Departamento de Astronomía, Universidad de Chile, Casilla 36-D, Santiago, Chile

⁸Centro de Astrofísica y Tecnologías Afines (CATA), Casilla 36-D, Santiago, Chile

⁹Astrophysics Research Centre, School of Mathematics and Physics, Queen's University Belfast, Belfast BT7 1NN, UK

¹⁰Observatoire Astronomique de l'Université de Genève, 51 Ch. des Maillettes, CH-1290 Versoix, Switzerland

Accepted 2018 April 6. Received 2018 February 28; in original form 2017 December 1

ABSTRACT

We present high cadence detections of two superflares from a bright G8 star ($V = 11.56$) with the Next Generation Transit Survey (NGTS). We improve upon previous superflare detections by resolving the flare rise and peak, allowing us to fit a solar flare inspired model without the need for arbitrary break points between rise and decay. Our data also enables us to identify substructure in the flares. From changing star-spot modulation in the NGTS data, we detect a stellar rotation period of 59 h, along with evidence for differential rotation. We combine this rotation period with the observed *ROSAT* X-ray flux to determine that the star's X-ray activity is saturated. We calculate the flare bolometric energies as $5.4^{+0.8}_{-0.7} \times 10^{34}$ and $2.6^{+0.4}_{-0.3} \times 10^{34}$ erg and compare our detections with G star superflares detected in the *Kepler* survey. We find our main flare to be one of the largest amplitude superflares detected from a bright G star. With energies more than 100 times greater than the Carrington event, our flare detections demonstrate the role that ground-based instruments such as NGTS can have in assessing the habitability of Earth-like exoplanets, particularly in the era of *PLATO*.

Key words: stars: activity – stars: flare – stars: individual: NGTS J030834.9–211322 – stars: rotation.

1 INTRODUCTION

Stellar flares are explosive phenomena caused by reconnection events in a star's magnetic field (e.g. Benz & Güdel 2010). When previously observed from the ground, they have been synonymous with active M stars, which flare regularly and brightly compared to their quiescent flux. Yet it is well known that the Sun shows regular flaring behaviour, with flares being detected over a wide range of energies. These range from 10^{23} erg for 'nanoflares' (Parnell & Jupp

2000) up to approximately 10^{32} erg for the largest occurrences such as the Carrington event (Carrington 1859; Hodgson 1859; Tsurutani et al. 2003). Observations of solar-type stars, mainly with *Kepler*, have shown that much more energetic 'superflares' of bolometric energies 10^{33} to 10^{36} erg are also possible (e.g. Shibayama et al. 2013).

The discovery of Earth-sized exoplanets in the habitable zones of their host stars (e.g. TRAPPIST-1 and Proxima Centauri; Anglada-Escudé et al. 2016; Gillon et al. 2017) has given renewed importance to these superflares, in particular their effects on exoplanet habitability (e.g. Lingam & Loeb 2017). Previous studies have found that the increase in UV radiation associated with flares can result in ozone

* E-mail: j.jackman@warwick.ac.uk

depletion (Segura et al. 2010), changes to atmospheric composition (Venot et al. 2016) and even biological damage (e.g. Estrela & Valio 2017). These effects are relatively well studied for M dwarf hosts, however it is expected that in future *PLATO* (Rauer et al. 2014) will reveal habitable zone planets around K and G stars. Compared to flares from later-type counterparts, detections of superflares from G stars are relatively rare. To date, no G star superflares have been detected with a CCD detector from the ground, although several have been seen either visually, in photography or with vidicon detectors (Schaefer 1989; Schaefer, King & Deliyannis 2000).

In recent years, observations with the *Kepler* satellite (Borucki et al. 2010) have captured greater number of superflare events from G-type stars. These have been from both the long (30 min) and short (1 min) cadence modes. In the long cadence mode, Maehara et al. (2012) and Shibayama et al. (2013) found 365 and 1547 superflares from 148 and 279 G-type stars respectively. In the 1 min short cadence mode, 187 superflares from 23 solar-type stars were found by Maehara et al. (2015). From these detections, the statistical properties of superflares on G-type stars were considered, with Maehara et al. (2012) and Shibayama et al. (2013) finding a power-law distribution of occurrence rate against energy of superflares that is comparable to solar flares, and with Maehara et al. (2015) identifying a correlation between the e-folding flare duration (time from flare amplitude peak to $1/e$ of its initial value) and the bolometric flare energy.

Candelaresi et al. (2014) also studied the occurrence rate of superflares from G dwarfs, as well as K and M dwarfs. They found the occurrence rate of superflares decreased with stellar effective temperature, and also peaked at a Rossby number of 0.1 (where Rossby number is the ratio of rotation period and convective turnover time). A Rossby number of 0.1 also corresponds to the rotation rate at which the X-ray emission of active stars saturates at 0.1 per cent of the bolometric luminosity (e.g. Pizzolato et al. 2003; Wright et al. 2011).

Previous studies have shown there may be a possible maximum limit on the energy that can be output by a G star superflare. Wu, Ip & Huang (2015) identified a saturation value of around 2×10^{37} erg, using stars in the sample of Maehara et al. (2012) that displayed periodic modulation. Similar saturation behaviour was detected by Davenport (2016) from their sample of 4041 flaring stars, for example, from the flaring G dwarf KIC 11551430. Davenport (2016) also found evidence for a weak correlation between flare luminosity and rotation period.

While these detections have shown the statistical properties of these white light flares, their temporal morphology and its link to solar flare morphology has not been investigated. This is due to the undersampling of the flare rise and peak from previous stellar flare surveys (mainly *Kepler*), particularly for shorter duration events. High cadence (< 1 min) data are required in order to compare observed solar flares and stellar superflares.

In this paper, we present the first ground-based CCD detections of superflares from a G-type star. These are some of the most well resolved superflares to date, with a higher cadence than all *Kepler* measurements and most ground-based observations. We present our measurements of the stellar and flare parameters and make comparisons with previously detected G star flares. We also present our modelling of each flare using a solar inspired general flare model.

2 OBSERVATIONS

The data presented in this paper were collected with the Next Generation Transit Survey (NGTS; Wheatley et al. 2018) over 80 nights

between 2015 November 4 and 2016 February 25. The two flares in this paper were detected on the nights of the 2015 December 17 and 2016 January 3. NGTS is a ground-based transiting exoplanet survey, operating at Paranal. It has 12, 20 cm f/2.8, optical telescopes, each with a 520–890 nm bandpass and exposure time of 10 s. Each single camera has a field of view of $\simeq 8$ deg². NGTS is designed to monitor bright ($I \leq 16$) K and M stars in the search for exoplanet transits (Wheatley et al. 2018). Unlike *Kepler*, NGTS observes without a set target list, meaning that all stars in our field of view that are bright enough can be studied. Each NGTS field is observed intensively whenever visible, and 3–4 fields are observed per telescope each year. With a total instantaneous field of view of 96 deg², and 10 s exposures, it is evident that NGTS is well suited to measure flare statistical distributions along with temporal morphology.

3 DATA ANALYSIS AND RESULTS

3.1 Flare search algorithm

When searching for flares, we started from the raw NGTS light curves and detrended them using a custom version of the *SYSTEM* algorithm (Mazeh, Tamuz & Zucker 2007). The full NGTS detrending is described by Wheatley et al. (2018). For these detrended light curves, we applied an additional filter to remove frames which showed excess variance above an empirically defined limit, primarily to remove data adversely affected by clouds. The time-scale of stellar flares is minutes to hours (e.g. Poletto 1989), so most flares will have duration less than one night, and we searched for flares on a night-by-night basis.

In order to find flares in each night, we searched for 3 consecutive points greater than 6 MAD from the median of the night, where MAD is the median absolute deviation. We have chosen MAD as it is a robust measure of the variation within a night, and it is typically not strongly biased by the flare itself (a separate search is also carried out for flares that dominate the whole night). We applied no binning to the data, in order to fully utilize the time resolution of NGTS. Once the automated flagging procedure was complete, we inspected each flagged night visually and removed false positives. Examples of events which resulted in false positive flags include satellites passing through our aperture and high amplitude variable stars (e.g. RR Lyrae).

3.2 Flare detection

Using the method from Section 3.1 we detected a single flare, shown in Fig. 1, from the star NGTS J030834.9–211322 (NGTS J0308–2113). This star has also previously been identified as 2MASS J03083496–2113222. After identifying this flare we visually inspected each night to search for lower amplitude flares which were not flagged. From this, we identified a second flare, shown in Fig. 2.

To confirm the flares were not from a neighbouring source, we checked individual NGTS images from before and during the large flare, along with the positions of nearby stars from *Gaia* and 2MASS. The nearest source identified is from *Gaia*, a 20.658 magnitude star 10.5 arcsec (2.1 pixels) away, placing it within our aperture. However, NGTS images reveal no shift in centroid position during the flare, and no light entering from outside the aperture, making us confident that the flares are from NGTS J0308–2113.

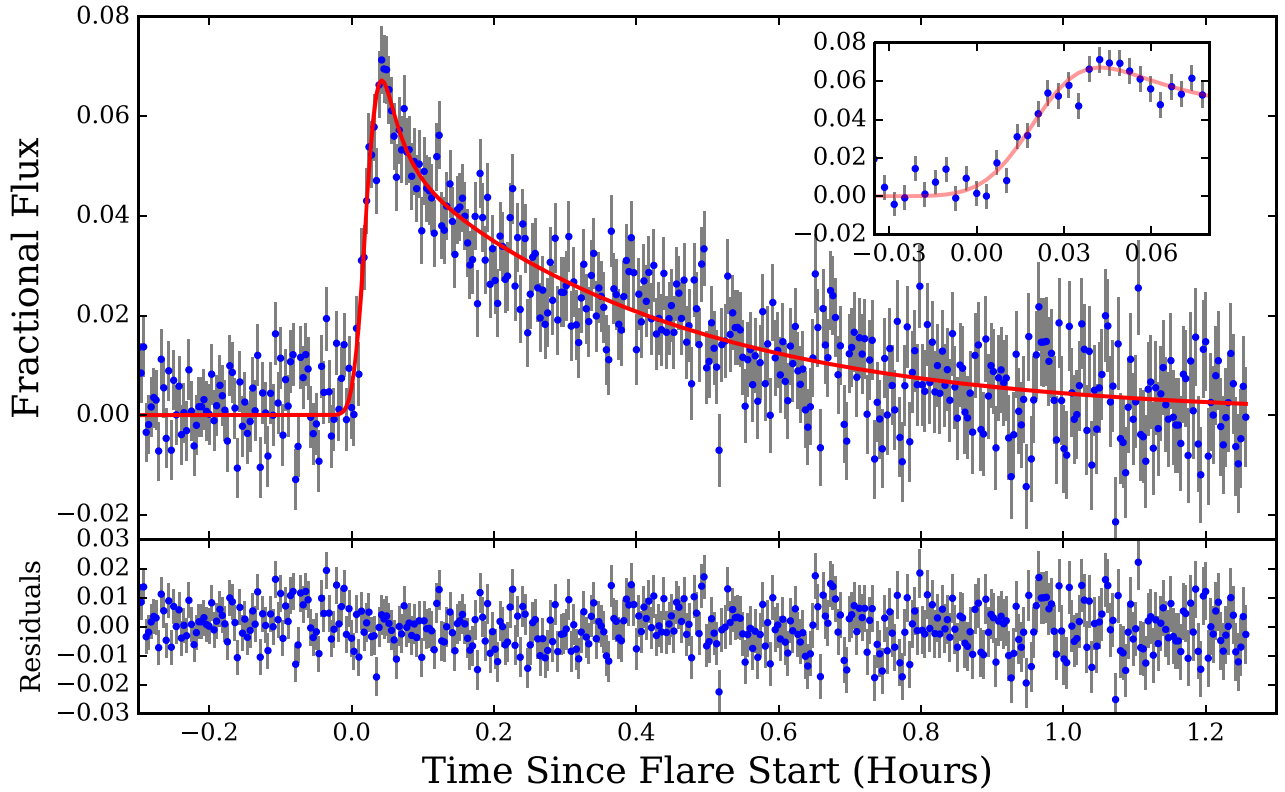


Figure 1. The superflare observed on NGTS J0308–2113 on 2016 January 3 with best-fitting model overlaid in red. The inset panel shows a zoomed in view of the data comprising the flare rise and peak, showing how the high cadence of NGTS has enabled us to resolve and fit to these regions. The bottom panel shows the residuals from our fitting. We note potential substructure in the flare decay around 0.7 h and discuss this in Section 4.

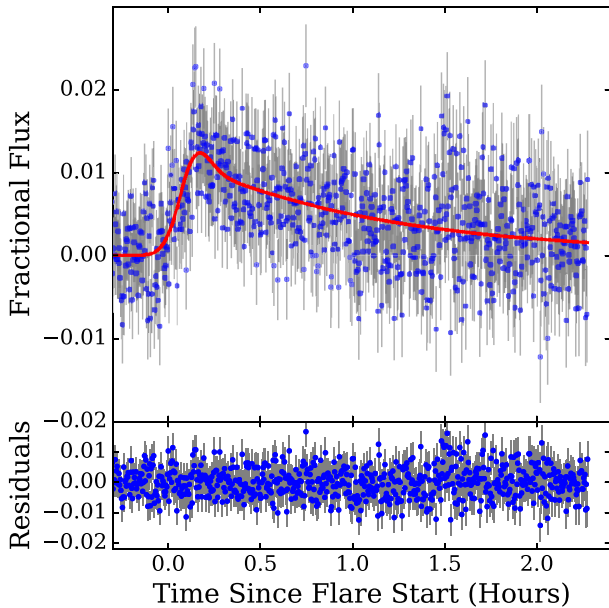


Figure 2. A lower amplitude flare, from 2015 December 17. The best-fitting model is overlaid in red. We note the appearance of substructure at the flare peak and at 1.5 h and discuss this in Section 4. The flare start time is given here by where the fit goes above 1σ above the quiescent flux, as discussed in Section 3.6.1

3.3 Stellar properties

To determine the stellar parameters for NGTS J0308–2113, we performed SED fitting using the broad-band photometry listed in Table 1. These photometric values were obtained as part of the standard NGTS cross-matching pipeline (Wheatley et al. 2018). We use the SED modelling method described in Gillen et al. (2017), with the BT-SETTL and PHOENIX v2 model atmospheres. The SED fit is shown in Fig. 3. We see no IR-excess that might indicate NGTS J0308–2113 is a pre-main-sequence star. From the SED fit, we determine the effective temperature $T_{\text{eff}} = 5458^{+108}_{-85}$ K. We then use the information presented in table 5 of Peca & Mamajek (2013) to identify the spectral type as G8. As a check on the spectral type we can also use the stellar colours with tables 3 and 4 of Covey et al. (2007), which confirm the G8 spectral type. To determine the stellar radius, we assume the star is main sequence and use the empirical radius–temperature relation from equation (8) of Boyajian et al. (2012, 2017), determined from mass–radius calculations for 33 stars of spectral type between G5V and M5.5V. We calculate our stellar radius as $0.81 \pm 0.04 R_{\odot}$. To estimate the uncertainty on the radius we use the median absolute deviation of $0.031 R_{\odot}$ from the Boyajian et al. (2012) fit and combine it with the upper error for our stellar temperature.

To check this source was not a giant star, we have compared the reduced proper motion, H_J against $J - H$ colour (e.g. Gould & Morgan 2003). Using the proper motion values from Table 1, we calculate $H_J = -0.78$ and $J - H = 0.35$. We use the criteria for dwarf/giant classification from Collier Cameron et al. (2007) to rule out the possibility that this star is a giant.

Table 1. Properties of NGTS J0308–2113. Coordinates are given in the J2000 system. References are as follows: 1. Skrutskie et al. (2006), 2. Gaia Collaboration (2016), 3. Henden & Munari (2014), 4. Cutri & et al. (2014), 5. Martin et al. (2005), 6. Boller et al. (2016), 7. Zacharias, Finch & Frouard (2017). *NUV*, *FUV*, *i'*, *r'*, *g'* are AB magnitudes. Proper motions are in mas yr^{−1}.

Property	Value	Reference
RA _{NGTS}	03:08:34.9	
Dec _{NGTS}	−21:13:22	
RA _{NGTS} (deg)	47.14557	
Dec _{NGTS} (deg)	−21.22284	
W4	8.773	4
W3	9.699	4
W2	9.731	4
W1	9.699	4
<i>K_s</i>	9.768	1
<i>H</i>	9.865	1
<i>J</i>	10.216	1
<i>i'</i>	11.174	3
<i>r'</i>	11.356	3
<i>g'</i>	11.899	3
<i>Gaia G</i>	11.354	2
<i>V</i>	11.562	3
<i>B</i>	12.291	3
<i>NUV</i>	16.943	5
<i>FUV</i>	20.666	5
<i>ROSAT</i> X-ray count rate (ct s ^{−1})	0.042	6
μ_{RA}	-1.2 ± 1.1	7
μ_{Dec}	-6.2 ± 1.1	7

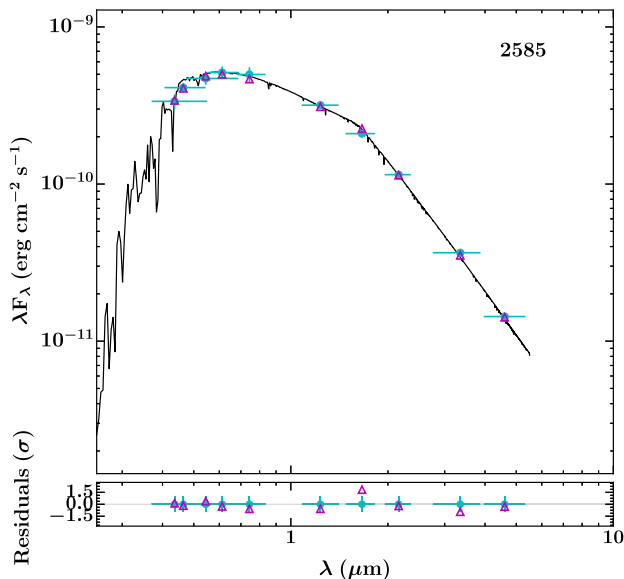


Figure 3. SED fit of NGTS J0308–2113 using the magnitudes listed in Table 1, matching best to a G8 spectral type.

We also note that this star was detected in X-rays with *ROSAT*. The detection of X-rays from this source is a sign of an active stellar corona (Boller et al. 2016).

3.4 Stellar rotation

The NGTS light curve of NGTS J0308–2113 shows periodic flux variations, which we attribute to star-spots moving across the visible

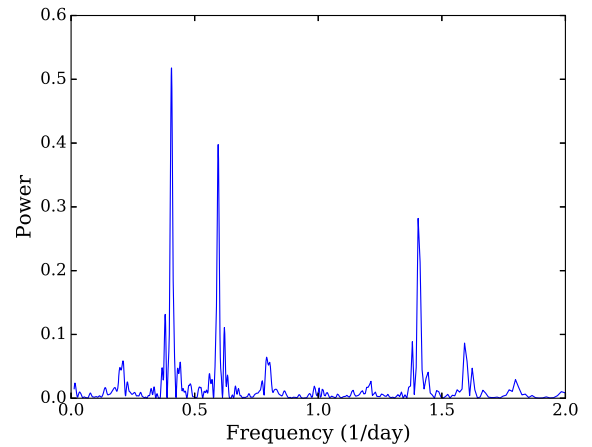


Figure 4. Lomb–Scargle periodogram for our full light curve. Here we show frequencies between 0 and 2 d^{−1}. Note the 1 d alias of the peak groups. The largest peak corresponds to our detected 59 h period.

disc of the star. We use this behaviour to determine the rotation period of the star, using a Lomb–Scargle periodogram. To do this, we use the *ASTROPY* package *LombScargle* (Astropy Collaboration 2013) and test for 20 000 periods spaced between 13 s and 80 d. We mask the flares from our light curve when performing this analysis. Our periodogram for the whole time series of NGTS J0308–2113 is shown in Fig. 4, from which the period of the main peak is 59.09 ± 0.01 h (0.41 d^{−1}). We calculate the uncertainty on this period by fitting a sine wave to the data. Using the analysis from Baluev (2008), we determine the false alarm probability of this peak to be negligible, a result of the high amount of data. We also note a second peak at 40 h, which we found to be an alias by performing an identical Lomb–Scargle analysis on a sine wave of period 59 h with the same time sampling as our light curve.

This short spin period implies that NGTS J0308–2113 must be a relatively young star, most likely less than ~ 600 Myr old, through comparing to the observed spin–age relations of open clusters (e.g. Stauffer et al. 2016; Douglas et al. 2017; Sadeghi Ardestani, Guillot & Morel 2017).

The amplitude of the observed spin modulation evolves with time. We split the light curve into three regions of activity, corresponding to an initial active portion, a secondary quiet portion and a final region where the amplitude increases once more. The 59 h period phase folded data for these regions can be seen in Fig. 5.

These regions are plotted in phase relative to the beginning of the light curve. The third region has a similar but slightly offset phase from the first, as well as less complete phase coverage due to a shorter duration. The duration of each region in the light curve are 40, 23, and 17 d, respectively. The change in phase, along with the changing flux variation, can be explained by the decay of the original set of star-spots and the formation of new ones. Star-spot lifetimes have been studied by Bradshaw & Hartigan (2014) and for main-sequence stars are on month time-scales. One example is CoRoT-2, which has a star-spot evolution time-scale of 31 ± 15 d (Silva-Valio & Lanza 2011). Consequently we attribute our changing light curve modulation to star-spot evolution.

We have also searched for periodic signals separately in the three light curve regions. The three Lomb–Scargle periodograms are presented in Fig. 6. In the second, quiet, period of the light curve we see no evidence for periodic modulation. Calculating the modulation period of the third region gives a significantly longer rotation period of 60.87 ± 0.04 h (0.39 d^{−1}). This offset period suggests that

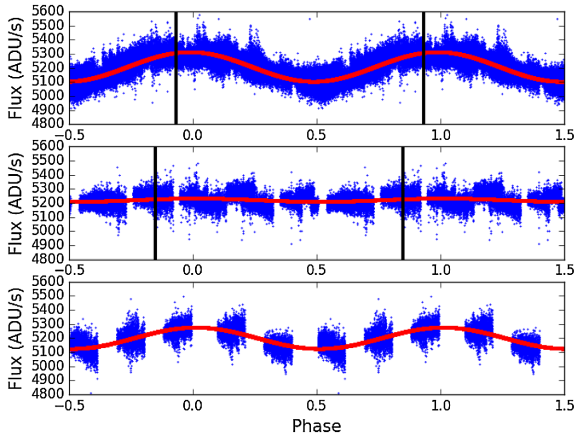


Figure 5. Phase folded data for the three regions of flux variation. Top is the initial active portion, middle is the quiet region and bottom is the following increase in activity. Overlaid in red is the sinusoidal fit for a 59 h period. The black lines indicate the location of the small flare (top section) and the large flare (middle section).

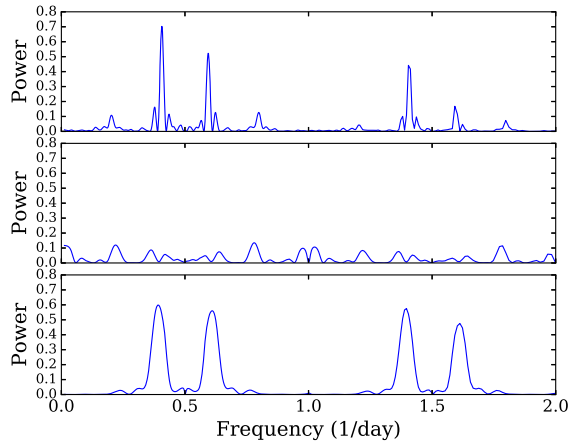


Figure 6. Lomb–Scargle periodograms for each section shown in Fig. 5. Note the lack of a period detection in the quiescent region.

the star exhibits differential rotation and that the new set of star-spots is formed at a different latitude to the original active region.

We also check where each flare occurs in phase, to search for any relation to the location of the active region. The smaller flare occurs towards the end of the first region, close to the maximum optical brightness, while the larger flare occurs in the second, quiet region at similar rotation phase (see Fig. 5). For the smaller flare, this is opposite in phase to the dominant active region. Neither flare seems to be located at a rotation phase where a large star-spot group is obviously visible, and we discuss this further in Section 4.

3.5 X-ray activity

As noted in Section 3.3, NGTS J0308–2113 has been detected in X-rays with *ROSAT*. The detection was made during the *ROSAT* all sky survey, and we have adopted count rates and hardness ratios from the 2RXS catalogue (Boller et al. 2016). The *ROSAT* PSPC count rate was $0.042 \pm 0.018 \text{ s}^{-1}$ and the hardness ratios in the standard *ROSAT* bands were $\text{HR1} = 1.000 \pm 0.325$ and $\text{HR2} = -0.428 \pm 0.243$. The HR1 value indicates that the source was

detected only in the *ROSAT* hard X-ray band (0.5–2.0 keV) and not in the soft band (0.1–0.4 keV).

The *ROSAT* PSPC count rate of NGTS J0308–2113 corresponds to a 0.1–2.4 keV energy flux of $5.7 \times 10^{-13} \text{ erg s}^{-1} \text{ cm}^{-2}$, using energy flux conversion factors determined for coronal sources by Fleming et al. (1995). This flux conversion uses the HR1 hardness ratio to account of the characteristic temperature of corona, and it has been applied to large samples of stars from the *ROSAT* all sky survey by Schmitt, Fleming & Giampapa (1995) and Huensch, Schmitt & Voges (1998).

This X-ray flux corresponds to a 0.1–2.4 keV X-ray luminosity of $L_X = 1.7 \times 10^{30} \text{ erg s}^{-1}$, assuming a distance to NGTS J0308–2113 of 156 pc that we estimate using the apparent *V* magnitude and the expected absolute *V* magnitude for a G8V star (Gray & Corbally 2009). Using the values for T_{eff} and R_* from Section 3.3 we find the bolometric luminosity of the star to be $L_{\text{Bol}} = 1.8 \times 10^{33} \text{ erg s}^{-1}$ and hence $\log L_X/L_{\text{Bol}} = -3.1$, which corresponds to saturated X-ray emission (Pizzolato et al. 2003; Wright et al. 2011).

Combining this X-ray luminosity with our measurement of the stellar rotation period (Section 3.4), we can place NGTS J0308–2113 on the rotation–activity relation of Wright et al. (2011). This is shown in Fig. 7 where NGTS J0308–2113 can be seen to reside close to the break point between saturated X-ray emission and the power law decrease in activity to slower rotation. The Rossby number of 0.18 was calculated using our rotation period and the relation for convective turnover time from Wright et al. (2011).

Using the relation between the X-ray surface flux and average coronal temperature from Johnstone & Güdel (2015), we estimate an average coronal temperature of 10 MK. This is similar to the coronal temperature of 7.5 MK predicted from the rotation period using the relation by Telleschi et al. (2005).

The lack of detection of NGTS J0308–2113 in the *ROSAT* soft band, as well as its relatively large distance, suggests that it may be subject to stronger interstellar absorption than the sample of stars used to determine the flux conversion factors of Fleming et al. (1995). We therefore double checked our flux estimation using WEBPIMMS.¹ We assumed a characteristic coronal temperature of 7.5 MK and an interstellar column density equal to the total Galactic column the direction of NGTS J0308–2113, which is $N_H = 2 \times 10^{20} \text{ cm}^{-2}$ (Dickey & Lockman 1990; Kalberla et al. 2005). The measured *ROSAT* PSPC count rate then corresponds to an unabsorbed 0.1–2.4 keV energy flux of $4.9 \times 10^{-13} \text{ erg cm}^{-2} \text{ s}^{-1}$, which is within 20 per cent of our calculation using the flux conversion factors of Fleming et al. (1995).

3.6 Flare modelling

We model our flares following a similar method to Gryciuk et al. (2017), who fitted solar flares in soft X-rays. For both flares, we use the convolution of a Gaussian with a double exponential. A Gaussian is used to account for the heating in the flare rise, which has been found to be appropriate for solar flares (e.g. Aschwanden, Dennis & Benz 1998). A double exponential is used for the decay, accounting for thermal and non-thermal cooling processes, which has been used previously for the decay of stellar flares (e.g. Davenport et al. 2014). A convolution of these Gaussian and exponential functions is then analogous to the heating and cooling processes occurring during the flare (Gryciuk et al. 2017). With this physically motivated model, we can utilize the high cadence of NGTS, in particular the flare rise

¹<https://heasarc.gsfc.nasa.gov/cgi-bin/Tools/w3pimms/w3pimms.pl>

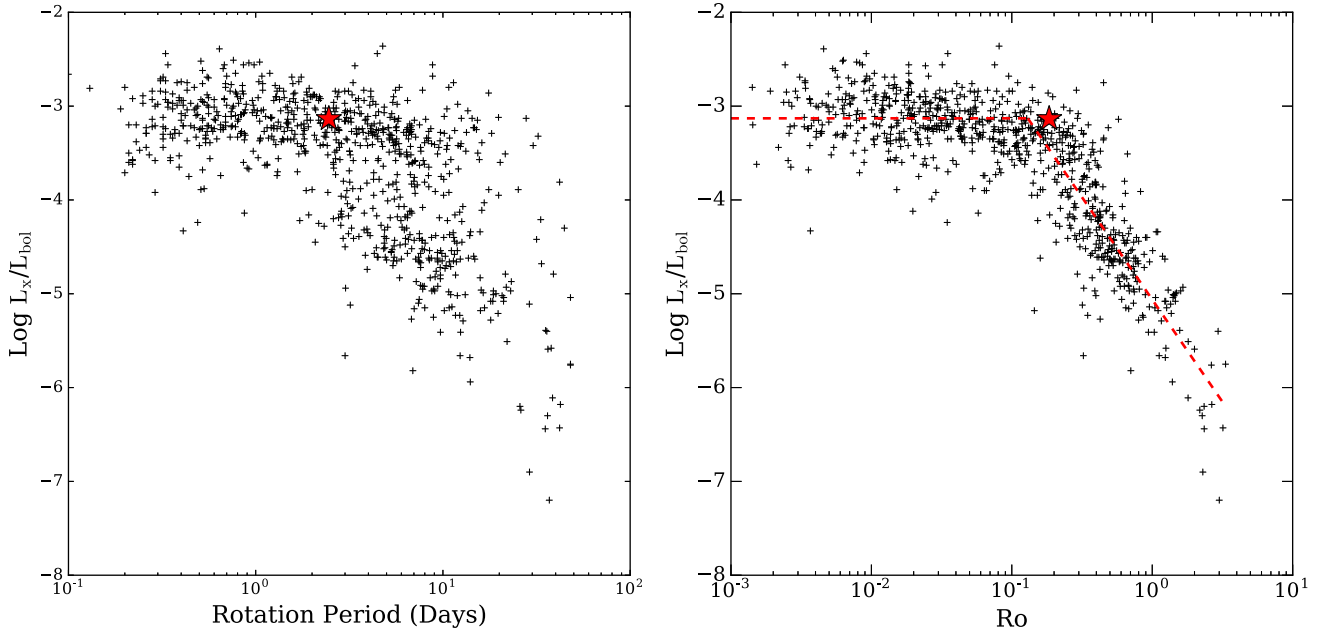


Figure 7. Left: Stellar X-ray to bolometric luminosity ratio versus rotation period for NGTS J0308–2113 with the data from Wright et al. (2011). Right: Same, but for Rossby number. We have also overlaid the power-law fit from Wright et al. (2011), with $\beta = -2.18$. NGTS J0308–2113 is shown here with a red star.

which in the past has been fit using a polynomial or disregarded due to a lack of data points (e.g. Davenport et al. 2014; Pugh et al. 2016).

Before performing fitting, we have inspected the full light curve and noted that several nights exhibited behaviour consistent with atmospheric extinction. We identified this trend by using the full light curve to fit for a first-order atmospheric extinction term. This trend was then removed from the light curve, including the nights showing our flares. The nights before and after each flare were used to check the quality of this fit and were found to have the atmospheric extinction successfully removed. We also account for the flux modulation effects from star-spots. To do this, we use the preceding two and subsequent two nights and fit a sinusoid at the calculated 59 h stellar rotation period. With this sinusoid, we are able to remove any gradient due to rotation from the night. This is required most for the smaller flare, which sits in the first, more active region of the light curve (Section 3.4).

For both flares, we perform fitting using an MCMC analysis with the python package *emcee* (Foreman-Mackey et al. 2013), using 500 walkers for 2000 steps and discarding the first 500 as a burn-in. During modelling we have increased our error bars to account for the scintillation using the modified Young’s approximation with the empirical coefficient for Paranal (Young 1967; Osborn et al. 2015). The best-fitting models for the two flares are overlaid on Figs 1 and 2. The best-fitting parameters presented in Table 2.

3.6.1 Flare amplitude and duration

To determine the amplitude of each flare, we use the maximum value of our fit. For the larger flare, this gives a fractional amplitude of 6.9 per cent. For the smaller flare, using the value from the fit gives a fractional amplitude of 1.2 per cent. Inspecting Fig. 2, there appears to be an impulsive substructure at the flare peak, which is not accounted for in our model. Taking the average of the five data points around the peak gives a peak amplitude of 2.0 ± 0.3 per cent.

Table 2. Properties of each superflare detected from NGTS J0308–2113.

Property	Large	Small
Energy (erg)	$5.4^{+0.8}_{-0.7} \times 10^{34}$	$2.6^{+0.4}_{-0.3} \times 10^{34}$
Fit amplitude (per cent)	6.9	1.2
Full duration (min)	55	N/A
e-folding duration (min)	16	55.5
Scale time (min)	11	42
Flare rise (min)	2.5	>7.4

To obtain a measure of the full duration of the flare, we again make use of our fit. We define the start and end of the flare as the points where the model rises and then falls more than 1σ above the background flux level, as in Gryciuk et al. (2017). Here σ is determined from the quiescent flux before the flare. From this, we determine the flare duration of the larger flare to be 55 min. Due to the decreased amplitude to error ratio of the smaller flare, we do not calculate the full flare duration using this method. However, we also calculate the flare duration with two additional methods – using its e-folding time-scale (as performed in Shibayama et al. 2013) and its scale time (the duration where the flare is above half the maximum flux value). Again, we use our fit for these. For the large and small flare, we calculate the e-folding time-scale as 16 and 55.5 min, respectively, and the scale time as 11 and 42 min, respectively. With our fit, we can also calculate the time-scale of the flare rise, using the time from the flare start to the peak of the model. Using this, we calculate the flare rise time as 2.5 min for the larger flare. If we use the 1σ start limit for the smaller flare, we estimate the flare rise as at least 7.4 min.

3.7 Flare energy

The method used to calculate the flare energy is based on that described by Shibayama et al. (2013), and makes the assumption that the flare and star act as blackbody radiators, with the flare having

a blackbody spectrum of temperature 9000 ± 500 K in order to estimate the flare luminosity. Using the stellar effective temperature and radius from Section 3.3, we calculate the bolometric energy of the larger and smaller flare to be $5.4^{+0.8}_{-0.7} \times 10^{34}$ and $2.6^{+0.4}_{-0.3} \times 10^{34}$ erg, respectively. It is striking that the smaller flare is only a factor 2 less energetic despite having an amplitude around six times lower. Comparing to the Carrington event energy of $\approx 10^{32}$ ergs (Tsurutani et al. 2003), we can see that each flare has a bolometric energy several hundred times greater than this.

From a total of 422 h of observation for this star, we have detected two flares. We can use this measurement to estimate the flaring rate for flares above $2.6^{+0.4}_{-0.3} \times 10^{34}$ erg as approximately 40 per year.

4 DISCUSSION

4.1 Flare properties

We have detected two superflares from the G star NGTS J0308–2113 with high cadence NGTS optical photometry. These are the first ground-based CCD detections of superflares from a G star. Our NGTS observations have much higher cadence than the *Kepler* flare detections, allowing us to resolve the flare rise and substructure.

The larger flare is shown in Fig. 1 and was calculated to have a bolometric energy of $5.4^{+0.8}_{-0.7} \times 10^{34}$ erg and a fractional amplitude of 6.9 per cent. Due to the increased time resolution of our measurements compared to almost all previous superflare detections, we have been able to fit this flare with a physically motivated model that includes a Gaussian pulse to describe the impulsive flare rise (as employed previously for solar flares). For the decay, our data require two exponential components. Separate impulsive and gradual decay components have been seen previously in some stellar flares, and attributed to decay of blackbody-like emission and chromospheric emission, respectively (Kowalski et al. 2013; Hawley et al. 2014). We can also see that this flare displays a flattening around the peak, or a ‘roll-over’. Similar flare peak behaviour has been seen by Kowalski et al. (2011) from ULTRACAM observations of the dM3.5e star EQ Peg A. This behaviour is captured in the fitted model as a result of the observed combination of Gaussian heating and exponential cooling. Further, we can identify smaller peaks in the decay of the flare, located at approximately 0.7 and 1.0 h after the flare starts in Fig. 1. Structure, or ‘bumps’, such as this have been previously identified in flare decays with *Kepler* (e.g. Balona et al. 2015).

Our model has also been used to fit the smaller flare of NGTS J0308–2113, shown in Fig. 2. This flare has a much lower relative amplitude of just 1.2 per cent, making it the lowest amplitude G star flare to have been detected from the ground. Despite its low amplitude, this smaller flare has a much slower rise and a longer duration than the larger flare (by factors of 3–4) so that it has a high total energy of $2.6^{+0.4}_{-0.3} \times 10^{34}$ erg, which is only a factor 2 lower than the larger flare. When fitting this smaller flare it became apparent that there was an additional structure at the flare peak. This can be seen in the residuals of Fig. 2, as a small spike lasting approximately 1 min. This is a sign of an additional heating pulse at the end of the initial flare rise. In this flare, we also detect substructure around 1.5 h after the flare start (visible in the residuals). The amplitude of the peak at this time is approximately 1 per cent, which is comparable with the amplitude of the main flare. Considering the timing of this substructure relative to the main flare peak, it is likely an example of sympathetic flaring (e.g. Moon et al. 2002).

One advantage of our flare model, combining a Gaussian heating pulse with exponential cooling, is that it avoids an arbitrary discontinuity between the end of the rise and the beginning of the decay. This has generally not been the case with previous stellar flare models, which tend to include an instantaneous transition between functions describing the rise and decay (e.g. Davenport et al. 2014). Our model also provides a well-defined measure of the rise time-scale, allowing for studies of how the flare rise time changes between flares. In this case, we see the lower amplitude flare rising much more slowly than the high amplitude example. This highlights how wide-field high cadence surveys such as NGTS can contribute to the quantitative characterization of stellar flares.

4.2 Star-spots and flare phases

Our analysis of the NGTS light curve of NGTS J0308–2113 revealed a 59.09 ± 0.01 h periodic modulation that we interpret the changing visibility of star-spots on the stellar rotation period (Section 3.4). The initial set of star-spots appear to decay during the observations, and no spin modulation is detected for an interval of around 23 d. Periodic modulation begins again towards the end of the NGTS observations, and at a slightly longer period, suggesting that the star exhibits differential rotation and that new star-spots have emerged at a different latitude.

Checking where the flares occur in rotation phase reveals that the smallest flare occurs in antiphase to the dominant star-spot group, while the largest flare occurs during the quiescent interval of the light curve (at a similar spin phase to the first flare). These flare timings are perhaps surprising, as we might expect to see superflares when large active regions are present and visible. Instead, our results suggest that the observed superflares do not emerge from the dominant active regions on the stellar surface. Such behaviour is not unprecedented, as observations of the M dwarfs AD Leo and GJ 1243 showed no correlation between stellar flare occurrence and rotational phase (Hunt-Walker et al. 2012; Hawley et al. 2014). A similar result was found for the K dwarf KIC 5110407, with all but the two strongest flares showing no correlation with the most active regions (Roettenbacher et al. 2013). In these cases, it was suggested that the dominant active region might be located at the pole, such that it is always in view and flares can be seen at any spin phase. An alternative is that the majority of flares originate from smaller spot groups that do not cause the dominant flux modulation.

4.3 Comparison with *Kepler*

In Fig. 8, we compare the superflares of NGTS J0308–2113 with G star superflares detected with *Kepler*. We use the samples from Shibayama et al. (2013) and Maehara et al. (2015) for the long and short cadence *Kepler* data, respectively. NGTS J0308–2113 has a *Kepler* magnitude of 11.4, calculated using the stellar g' and r' magnitudes and equation 2a from Brown et al. (2011). This magnitude makes it one of the brightest G stars seen to exhibit a superflare (see Fig. 8). The larger flare from NGTS J0308–2113 also has a greater amplitude than all but one of those detected in short cadence *Kepler* data. This flare also has a shorter duration than most detected with *Kepler*. This comparison demonstrates that NGTS has a sufficiently wide-field of view and high photometric precision to detect rare and interesting stellar flares from bright stars. Each flare is also observed with higher cadence than has previously been possible.

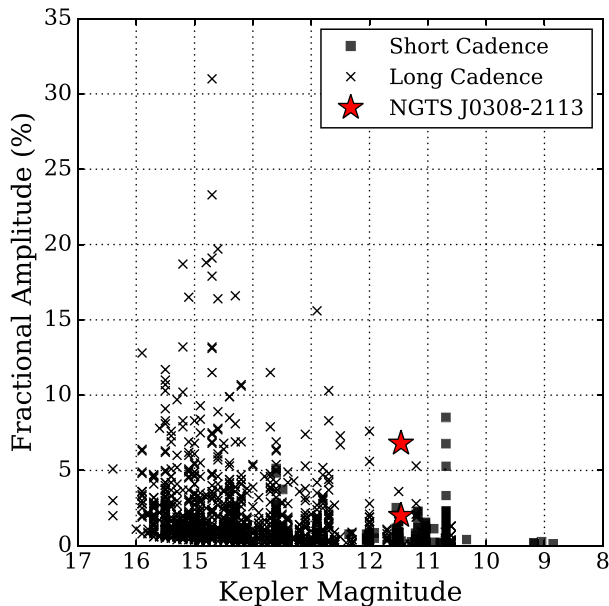


Figure 8. Comparison of the fractional amplitudes and *Kepler* magnitude of our flares from NGTS J0308–2113 (red stars) with G star superflares detected in short cadence (black squares) and long cadence (black crosses) *Kepler* data. When comparing fractional amplitudes between NGTS and *Kepler*, it should be noted that the *Kepler* bandpass extends blueward of NGTS.

4.4 X-ray activity

Thanks to the relative proximity and hence brightness of NGTS J0308–2113, we were able to measure its X-ray luminosity using archival *ROSAT* data (Section 3.5). We found that the star is in the saturated X-ray regime, with $\log L_X/L_{\text{Bol}} = -3.1$, and that its X-ray emission is consistent with the rotation activity relation of Wright et al. (2011). It was not detected in the *ROSAT* soft X-ray band, likely due to interstellar absorption. Using our measured spin period and the relation for convective turnover time by Wright et al. (2011), we have estimated the Rossby number of NGTS J0308–2113 to be 0.18. Interestingly, this places the star close to the peak of superflare occurrence rates found by Candaresi et al. (2014).

We can also compare the X-ray luminosity of NGTS J0308–2113 with that of other G stars exhibiting superflares. Yabuki et al. (2017) found nine stars with X-ray detections from the *Kepler* superflare sample of Shibayama et al. (2013). Using these nine X-ray detections they identified a correlation between the largest white-light flare energies (estimated from *Kepler* data) and quiescent L_X with

$$E_{\text{Bol}} \propto L_X^{1.2 \pm 0.3}_{0.4} \quad (1)$$

Based on this relation, we would expect NGTS J0308–2113 to exhibit flares of energies up to approximately 8×10^{35} erg. This is around 13 times greater than the energy of our larger flare, suggesting NGTS J0308–2113 sometimes exhibits even more energetic flares than the examples we have detected with NGTS.

4.4.1 Maximum flare energy

An alternative method to estimate the potential maximum flare energy is to use the star-spot activity. This is done using equation 1

from Shibata et al. (2013),

$$E_{\text{flare}} \approx 7 \times 10^{32} (\text{erg}) \left(\frac{f}{0.1} \right) \left(\frac{B}{10^3 \text{ G}} \right)^2 \left(\frac{A_{\text{spot}}}{3 \times 10^{19} \text{ cm}^2} \right)^{3/2}, \quad (2)$$

where f , B , and A_{spot} are the fraction of magnetic energy that can be released as flare energy and the magnetic field strength and area of the star-spot, respectively. We estimate the star-spot area from the light curve modulation normalized by the average brightness, following the method of Notsu et al. (2013). We use the region of greatest brightness variation to estimate the area, obtaining a value equivalent to 0.04 of the visible stellar surface. We assume $f = 0.1$ (Aschwanden, Xu & Jing 2014) and $B = 1000\text{--}3000\text{ G}$ (typical comparison values for solar-type stars, e.g. Solanki 2003; Maehara et al. 2015) and calculate $E_{\text{flare}} = 0.9\text{--}8.5 \times 10^{35}$ erg. This estimated value is the same order of magnitude as that calculated from the X-ray data, predicting a flare of greater energy than our largest event.

4.5 Implications for exoplanet habitability

Understanding the properties of superflares from G stars is important when considering the habitability of Earth-like exoplanets, including those expected to be detected with *PLATO* (Rauer et al. 2014). Stellar flares are known to be associated with intense ultraviolet radiation (e.g. Stelzer et al. 2006; Tsang et al. 2012), which can reduce levels of atmospheric ozone (e.g. Lingam & Loeb 2017) and damage the DNA of biological organisms (e.g. Castenholz & Garcia-Pichel 2012). Associated X-ray and extreme-ultraviolet radiation can also erode the planetary atmosphere and drive water loss. Stellar flares are also associated with coronal mass ejections (CMEs), and while planetary magnetospheres may protect against the quiescent stellar wind, CMEs can act to compress the magnetosphere and expose the planetary atmosphere to further erosion and desiccation (e.g. Lammer et al. 2007; Kay, Opher & Kornbleuth 2016).

The detections of superflares presented in this paper demonstrate that wide-field ground-based surveys such as NGTS are capable of characterizing the rates and energies of superflares from G-type stars, despite their relatively low fractional amplitude. Since flare detections with ground-based telescopes can be made and announced in real time, it may also be possible to trigger immediate follow up of superflares with larger narrow-field telescopes while the flares are still in progress. This has not been possible to date because of the unpredictable nature of superflares and inevitable delays in downlinking and processing data from space telescopes such as *Kepler*. Real-time follow up of NGTS flares might then provide the multiwavelength observations needed to assess the impact of superflares on potentially habitable exoplanet atmospheres.

5 CONCLUSIONS

In this work, we have presented the detection of two superflares from the G8 star NGTS J030834.9–211322 using NGTS. These are the first G star superflares detected from the ground using a CCD, and they are among the highest cadence measurements of any superflares to date. We fit both flares with a model that incorporates a Gaussian heating pulse, as seen previously in solar flares, and exponential decay on two time-scales. The model fit provides the amplitude, energy and duration of each flare, and we find the two flares have similar total energies despite their different amplitudes and durations. The larger flare has an unusually high amplitude and a short duration for a G star superflare. Our model also allows

us to measure the time-scale of the flare rise, an interval that has been undersampled in previous studies, and we find that the longer duration flare has a slower rise. We have also detected substructure in both flares.

The stellar rotation period of NGTS J0308–2113 was measured to be 59 h, and we found evidence for differential rotation. The X-ray luminosity of the star was calculated to be 1.7×10^{30} erg s^{−1}, with $\log L_X/L_{\text{Bol}} = -3.1$ implying saturated X-ray emission, as expected for a G8 star with such a short spin period. The Rossby number of 0.18 places NGTS J0308–2113 close to the peak of the occurrence rate distribution implied by previous flare detections.

Our results highlight the potential for wide-field ground-based surveys such as NGTS to determine the rates, energies, and morphologies of superflares from G stars, despite the modest white-light amplitudes of such flares. Further detections and real-time multi-wavelength follow up will be important in assessing the habitability of Earth-like exoplanets around G stars, including those to be found with *PLATO*.

ACKNOWLEDGEMENTS

This research is based on data collected under the *NGTS* project at the ESO La Silla Paranal Observatory. The NGTS facility is funded by a consortium of institutes consisting of the University of Warwick, the University of Leicester, Queen’s University Belfast, the University of Geneva, the Deutsches Zentrum für Luft- und Raumfahrt e.V. (DLR; under the ‘Großinvestition GI-NGTS’), the University of Cambridge, together with the UK Science and Technology Facilities Council (STFC; project reference ST/M001962/1). JAGJ is supported by an STFC studentship. PJW, DJA, and RGW are supported by STFC consolidated grant ST/P000495/1. AMB acknowledges the support of the Institute of Advanced Study, University of Warwick and is also supported by STFC consolidated grant ST/P000320/1. JSJ acknowledges support by Fondecyt grant 1161218 and partial support by CATA-Basal (PB06, CONICYT). MNG is supported by STFC award reference 1490409 as well as the Isaac Newton Studentship. CEP acknowledges support from the European Research Council under the SeismoSun Research Project No. 321141. The research leading to these results has received funding from the European Research Council under the European Union’s Seventh Framework Programme (FP/2007–2013)/ERC Grant Agreement no. 320964 (WDTracer).

REFERENCES

Anglada-Escudé G. et al., 2016, *Nature*, 536, 437
 Aschwanden M. J., Dennis B. R., Benz A. O., 1998, *ApJ*, 497, 972
 Aschwanden M. J., Xu Y., Jing J., 2014, *ApJ*, 797, 50
 Astropy Collaboration, 2013, *A&A*, 558, A33
 Balona L. A., Broomhall A.-M., Kosovichev A., Nakariakov V. M., Pugh C. E., Van Doorselaere T., 2015, *MNRAS*, 450, 956
 Baluev R. V., 2008, *MNRAS*, 385, 1279
 Benz A. O., Güdel M., 2010, *ARA&A*, 48, 241
 Boller T., Freyberg M. J., Trümper J., Haberl F., Voges W., Nandra K., 2016, *A&A*, 588, A103
 Borucki W. J. et al., 2010, *Science*, 327, 977
 Boyajian T. S. et al., 2012, *ApJ*, 757, 112
 Boyajian T. S. et al., 2017, *ApJ*, 845, 178
 Bradshaw S. J., Hartigan P., 2014, *ApJ*, 795, 79
 Brown T. M., Latham D. W., Everett M. E., Esquerdo G. A., 2011, *AJ*, 142, 112
 Candelaresi S., Hillier A., Maehara H., Brandenburg A., Shibata K., 2014, *ApJ*, 792, 67

Carrington R. C., 1859, *MNRAS*, 20, 13
 Castenholz R. W., Garcia-Pichel F., 2012, *Ecology of Cyanobacteria II*. Springer, Berlin, p. 481
 Collier Cameron A. et al., 2007, *MNRAS*, 380, 1230
 Covey K. R. et al., 2007, *AJ*, 134, 2398
 Cutri R. M. et al., 2014, *VizieR Online Data Catalog*, 2328
 Davenport J. R. A., 2016, *ApJ*, 829, 23
 Davenport J. R. A. et al., 2014, *ApJ*, 797, 122
 Dickey J. M., Lockman F. J., 1990, *ARA&A*, 28, 215
 Douglas S. T., Agüeros M. A., Covey K. R., Kraus A., 2017, *ApJ*, 842, 83
 Estrela R., Valio A., 2017, preprint ([arXiv:1708.05400](https://arxiv.org/abs/1708.05400))
 Fleming T. A., Molendi S., Maccacaro T., Wolter A., 1995, *ApJS*, 99, 701
 Foreman-Mackey D., Hogg D. W., Lang D., Goodman J., 2013, *PASP*, 125, 306
 Gaia Collaboration, 2016, *A&A*, 595, A2
 Gillen E., Hillenbrand L. A., David T. J., Aigrain S., Rebull L., Stauffer J., Cody A. M., Queloz D., 2017, *ApJ*, 849, 11
 Gillon M. et al., 2017, *Nature*, 542, 456
 Gould A., Morgan C. W., 2003, *ApJ*, 585, 1056
 Gray R. O., Corbally J. C., 2009, *Stellar Spectral Classification*. Princeton Univ. Press, Princeton, NJ
 Gryciuk M., Siarkowski M., Sylwester J., Gburek S., Podgorski P., Kepa A., Sylwester B., Mrozek T., 2017, *Sol. Phys.*, 292, 77
 Hawley S. L., Davenport J. R. A., Kowalski A. F., Wisniewski J. P., Hebb L., Deitrick R., Hilton E. J., 2014, *ApJ*, 797, 121
 Henden A., Munari U., 2014, *Contrib. Astron. Obs. Skalnaté Pleso*, 43, 518
 Hodgson R., 1859, *MNRAS*, 20, 15
 Huensch M., Schmitt J. H. M. M., Voges W., 1998, *A&AS*, 132, 155
 Hunt-Walker N. M., Hilton E. J., Kowalski A. F., Hawley S. L., Matthews J. M., 2012, *PASP*, 124, 545
 Johnstone C. P., Güdel M., 2015, *A&A*, 578, A129
 Kalberla P. M. W., Burton W. B., Hartmann D., Arnal E. M., Bajaja E., Morras R., Pöppel W. G. L., 2005, *A&A*, 440, 775
 Kay C., Opher M., Kornbleuth M., 2016, *ApJ*, 826, 195
 Kowalski A. F., Mathioudakis M., Hawley S. L., Hilton E. J., Dhillon V. S., Marsh T. R., Copperwheat C. M., 2011, in Johns-Krull C., Browning M. K., West A. A., eds, *ASP Conf. Ser. Vol. 448, 16th Cambridge Workshop on Cool Stars, Stellar Systems, and the Sun*. Astron. Soc. Pac., San Francisco, p. 1157
 Kowalski A. F., Hawley S. L., Wisniewski J. P., Osten R. A., Hilton E. J., Holtzman J. A., Schmidt S. J., Davenport J. R. A., 2013, *ApJS*, 207, 15
 Lammer H. et al., 2007, *Astrobiology*, 7, 185
 Lingam M., Loeb A., 2017, *ApJ*, 848, 41
 Maehara H. et al., 2012, *Nature*, 485, 478
 Maehara H., Shibayama T., Notsu Y., Notsu S., Honda S., Nogami D., Shibata K., 2015, *Earth Planets Space*, 67, 59
 Martin D. C. et al., 2005, *ApJ*, 619, L1
 Mazeh T., Tamuz O., Zucker S., 2007, in Afonso C., Weldrake D., Henning T., eds, *ASP Conf. Ser. Vol. 366, Transiting Extrapolar Planets Workshop*. Astron. Soc. Pac., San Francisco, p. 119
 Moon Y.-J., Choe G. S., Park Y. D., Wang H., Gallagher P. T., Chae J., Yun H. S., Goode P. R., 2002, *ApJ*, 574, 434
 Notsu Y. et al., 2013, *ApJ*, 771, 127
 Osborn J., Föhring D., Dhillon V. S., Wilson R. W., 2015, *MNRAS*, 452, 1707
 Parnell C. E., Jupp P. E., 2000, *ApJ*, 529, 554
 Pecaú M. J., Mamajek E. E., 2013, *ApJS*, 208, 9
 Pizzolato N., Maggio A., Micela G., Sciortino S., Ventura P., 2003, *A&A*, 397, 147
 Poletto G., 1989, *Sol. Phys.*, 121, 313
 Pugh C. E., Armstrong D. J., Nakariakov V. M., Broomhall A.-M., 2016, *MNRAS*, 459, 3659
 Rauer H. et al., 2014, *Exp. Astron.*, 38, 249
 Roettenbacher R. M., Monnier J. D., Harmon R. O., Barclay T., Still M., 2013, *ApJ*, 767, 60
 Sadehgi Ardestani L., Guillot T., Morel P., 2017, *MNRAS*, 472, 2590
 Schaefer B. E., 1989, *ApJ*, 337, 927
 Schaefer B. E., King J. R., Deliyannis C. P., 2000, *ApJ*, 529, 1026

- Schmitt J. H. M. M., Fleming T. A., Giampapa M. S., 1995, *ApJ*, 450, 392
- Segura A., Walkowicz L. M., Meadows V., Kasting J., Hawley S., 2010, *Astrobiology*, 10, 751
- Shibata K. et al., 2013, *PASJ*, 65, 49
- Shibayama T. et al., 2013, *ApJS*, 209, 5
- Silva-Valio A., Lanza A. F., 2011, *A&A*, 529, A36
- Skrutskie M. F. et al., 2006, *AJ*, 131, 1163
- Solanki S. K., 2003, *A&AR*, 11, 153
- Stauffer J. et al., 2016, *AJ*, 152, 115
- Stelzer B., Schmitt J. H. M. M., Micela G., Liefke C., 2006, *A&A*, 460, L35
- Telleschi A., Güdel M., Briggs K., Audard M., Ness J.-U., Skinner S. L., 2005, *ApJ*, 622, 653
- Tsang B. T. H., Pun C. S. J., Di Stefano R., Li K. L., Kong A. K. H., 2012, *ApJ*, 754, 107
- Tsurutani B. T., Gonzalez W. D., Lakhina G. S., Alex S., 2003, *J. Geophys. Res.: Space Phys.*, 108,
- Venot O., Rocchetto M., Carl S., Roshni Hashim A., Decin L., 2016, *ApJ*, 830, 77
- Wheatley P. J. et al., 2018, *MNRAS*, 475, 4476
- Wright N. J., Drake J. J., Mamajek E. E., Henry G. W., 2011, *ApJ*, 743, 48
- Wu C.-J., Ip W.-H., Huang L.-C., 2015, *ApJ*, 798, 92
- Yabuki K., Sasaki R., Sugawara Y., Katsuda S., Maehara H., 2017, in Serino M., Shidatsu M., Iwakiri W., Mihara T., eds, 7 Years of MAXI: Monitoring X-ray Transients. RIKEN, Saitama, Japan, p. 187. Available at: <https://indico2.riken.jp/indico/conferenceDisplay.py?confId=2357>
- Young A. T., 1967, *AJ*, 72, 747
- Zacharias N., Finch C., Frouard J., 2017, *AJ*, 153, 166

This paper has been typeset from a \TeX/L\AA\TeX file prepared by the author.